Meteorologische Zeitschrift, Vol. **11**, No. 1, 49-60 (February 2002)

Article

On Precipitation induced polarization of microwave radiation measured from space

HARALD CZEKALA[1,*] and CLEMENS SIMMER[2]

[1] NASA Goddard Institute for Space Studies, New York, USA
[2] Meteorologisches Institut der Universität Bonn, Germany

(Manuscript received August 15, 2000; accepted June 11, 2001)

Abstract

The polarization effects caused by horizontally aligned oblate hydrometeors show significant differences compared to the effect of spherical particles. Even in the presence of a thick ice cloud above the precipitation layer the oblate raindrops may still have an impact on the polarization differences $(T_{B,v} - T_{B,h})$ observed from space. For large oblate ice particles with aspect ratios as high as 3.3 the polarization difference is strongest for 85 GHz (more than 40 K). Other reasonable choices of ice particle shape above a layer of nonspherical rain drops can alter the results such that the polarization difference at 37 GHz exceeds the 85 GHz polarization signal, reaching +15 K for 37 GHz at a rain rate of 50 mm/h. The scattering signal at 85 GHz is very sensitive to ice mass, but also depends very much on the ice particle shape. By choosing different ice shapes we demonstrate the large range of polarization signatures that can be expected and which include the results reported in the literature. Since different rain events are probably associated with different kinds of ice particles, the 85 GHz scattering signature is a very ambiguous source of information if it is used without additional information. At low frequencies (below 37 GHz) there is hardly any sensitivity to the ice particle shape. The information is directly linked to the water mass and raindrop shape which is known to a much better extent than the ice particle shape.

Zusammenfassung

Die von horizontal angeordneten, abgeplatteten Hydrometeoren verursachten Polarisationseffekte, zeigen signifikante Unterschiede im Vergleich zu den Effekten bei sphärischen Partikeln. Selbst bei Vorhandensein einer dicken Eiswolke oberhalb des Niederschlagsniveaus können die abgeplatteten Regentropfen immer noch einen Einfluss auf die von Weltraum beobachteten Polarisationsdifferenzen $(T_{B,v} - T_{B,h})$ besitzen. Bei großen, flachen Eispartikeln mit einem Seitenverhältnis bis zu 3.3 ist die Polarisationsdifferenz bei 80 GHz (über 40 K) am stärksten. Andere, sinnvoll ausgewählte Eispartikelformen über der Schicht mit den nichtsphärischen Regentropfen können doe Ergebnisse dergestlat verändern, dass doe Polarisationsdifferenz bei 37 GHz das Signal der Polarisation bei 85 GHz übersteigen; sie erreichen +15 K bei 37 GHz und einer Regenintensität von 50 mm/h. Das Streusignal bei 85 GHz ist sehr empfindlich bezüglich der Masse des Eises, aber hängt auch sehr stark von der Form der Eispartikel ab. Durch die Wahl verschiedener Eisformen erklären wir den weiten Bereich der Polarisationssignaturen, der erwartet werden kann und Ergebnisse aus der Literatur umfasst. Unterschiedliche Regenereignisse rühren von unterschiedlichen Arten von Eispartikeln her. Somit ist die Signatur der Streuung bei 85 GHz eine sehr vieldeutige Informationsquelle, wenn sie ohne Zusatzinformation benutzt wird. Im Bereich niedriger Frequenzen (unter 37 GHz) findet man so gut wie keine Empfindlichkeit gegenüber der Eispartikelform. Die Information ist unmittelbar mit der Masse des Wassers und der Form der Regentropfen verbunden; letztere ist wesentlich besser bekannt als die Form der Eispartikel.

1 Introduction

Most algorithms for rain retrieval from passive microwave measurements from space are based on forward radiative transfer modeling. Thus the quality of these algorithms rely on the quality of the used radiative transfer models. The signals exploited by he derived algorithms differ depending on the surface conditions, namely ocean or land. Many algorithms rely directly or indirectly on the observed polarization differences at different frequencies. Over oceans the reduction of atmospheric transparency due to the hydrometeors reduces the large polarization generated by the ocean surface. Over land surfaces the combined effects of the reduction of radiation intensity due to both the screening of the strong surface emission and hydrometeor scattering is used at high frequencies as signals.

The atmospheric effects on microwave radiation consist of a well understood emission and absorption process by various gas species and the emission, absorption and scattering process by hydrometeors. While the gas interaction is unpolarized with no angular variation,

* Corresponding author: Harald Czekala, Department of Applied Physics and Applied Mathematics, Columbia University, NASA Goddard Institute for Space Studies, New York, 2880 Broadway, New York, NY 10025, USA, email: hczekala@giss.nasa.gov

0941-2948/02/0011-0049 $ 05.40
DOI: 10.1127/0941-2948/2002/0011-0049

the effects of hydrometeors exhibit a dependence on direction and polarization of radiation. Furthermore, they have a less predictable impact on the angular pattern of intensity and the state of polarization by themselves (e.g. LIU and SIMMER, 1996; CZEKALA and SIMMER, 1998; CZEKALA, 1998; HORNBOSTEL et al., 1999). These effects have not been taken into account in current retrieval algorithms.

In this paper we will explore by simple atmospheric setups the range of variability and uncertainty to be expected by the effects of emission, extinction, and scattering by taking into account the shape variability of large hydrometeors.

We will focus on some commonly used satellite frequencies and the corresponding down-looking viewing geometry. Low frequency radiation (e.g. below 37 GHz) tends to penetrate clouds and even moderate rain. These frequencies are mostly taken for emission based retrieval techniques over radiatively cold ocean surfaces. The amount of emitted radiation is largely determined by the liquid water path (LWP) for low frequencies with considerable transparency. With increasing opacity at higher frequencies (37 and 85 GHz) the vertical distribution of precipitation within the atmosphere (hydrometeor vertical profile) becomes more important, at least until moderate optical thicknesses. For higher optical depth the profile importance decreases due to transmission reduction, but the retrieval then will focus on the uppermost parts of the atmosphere. With the 85 GHz channels of the Special Sensor Microwave/Imager (SSM/I), launched on the Defense Meteorological Satellite Program (DMSP) satellites in 1987 for the first time, a considerably larger frequency is available for remote sensing of rain (PRABHAKARA et al., 1992; ADLER et al., 1993). Due to the larger size parameters (particle size compared to wavelength) the absorption by liquid water is much larger than in the low frequency range. This absorption saturates the emission signal already at the onset of rainfall at very low rain rates (RR). A retrieval of RR is still possible, however, through indirect measurement: Large RR are often associated with a significant ice mass above the raining cloud. These ice particles have an absorption coefficient two orders of magnitude lower than water and act like almost non-absorbing scatterers. Their size, which is comparable to the wavelength at 85 GHz, makes scattering very efficient. The brightness temperature depression caused by the ice scattering above rain layers is used to derive the corresponding rain rate.

Obviously, such methods require accurate modeling of the scattering process, which is affected also by shape and orientation of the hydrometeors (CZEKALA and SIMMER, 1998; CZEKALA, 1998; CZEKALA et al., 1999). While there has been some effort to use nonspherical ice particles, the effect of the liquid phase below has mostly been neglected. The attenuation of radio waves by realistically shaped raindrops had been considered already by OGUCHI (1960, 1964) and also by ASANO and YAMAMOTO (1975) more than 25 years ago. A study using oblate ice and rain was carried out by WU and WEINMAN (1984), but the radiative transfer aspects treated approximative. Their model used the nonspherical scattering coefficients in the EDDINGTON approximation which was solved independently for two orthogonal polarizations. Recently, there is a growing number of microwave models taking into account nonspherical particles in full vector radiative transfer calculations (HAFERMAN, 1999). However, they still assume either randomly oriented particles (HAFERMAN et al., 1997), or concentrate on ice particles above rain layers and cirrus particles at high frequencies (EVANS and STEPHENS, 1995a; EVANS et al., 1998). Our study will focus on the combined effect of rain and ice particle layers, both containing nonspherical particles.

Most precipitation algorithms use only the brightness temperature depression due to scattering and the depolarizing effects of hydrometeors on the polarization which originates from the sea surface. Although depolarizing due to hydrometeors is the dominant effect in amplitude, it is well known that multiple scattering by hydrometeors (even when using Lorenz-Mie theory for spherical particles) produces some amount of polarization by itself (LIU and SIMMER, 1996). Separate effects of liquid rain and non-precipitating ice clouds have already been demonstrated by CZEKALA and SIMMER (1998) and CZEKALA (1998), respectively. Here we will extend these studies to typical rain structures containing mixtures of liquid and frozen particles including non-precipitating cloud layers. We further extend the studies by using different surface conditions, ranging from highly polarizing surfaces to for non-polarizing surfaces.

Thus, the observed polarization in the presence of precipitation will always be a mixture of three components: (1) surface emitted polarization, (2) polarization due to liquid rain drops, (3) polarization due to ice particles above the rain layer. The aim of this study is to show that the complete understanding of the mixture of polarization contributions to the total satellite observed signal will be crucial for improving precipitation retrieval from space.

The following section will give a short outline of the required radiative transfer theory, followed by a short model description. For a complete review of theory and model see CZEKALA and SIMMER (1998). The effects of nonspherical hydrometeors in different model atmospheres are presented in Section 3, followed by a detailed discussion of the results in Section 4. Section 5 will summarize our conclusions.

2 Theoretical background

2.1 Vector radiative transfer

For a description of polarized radiation within an one-dimensional plane parallel atmosphere containing nonspherical particles of arbitrary orientation the vector

radiative transfer equation for the Stokes vector $\overline{\mathbf{I}} = (I_v, I_h, U, V)$ (VRTE, e.g. TSANG et al., 1985; HAFERMAN et al., 1997; EVANS and STEPHENS, 1995a)

$$\cos\theta \frac{d\overline{\mathbf{I}}(z,\theta)}{dz} = -\overline{\overline{\sigma}}_e(z,\theta)\,\overline{\mathbf{I}}(z,\theta) + \overline{\sigma}_a(z,\theta)\,B(T(z)) + \int_0^{\pi} \overline{\overline{\mathbf{P}}}(z,\theta;\theta')\,\overline{\mathbf{I}}(z,\theta')\,\sin\theta' d\theta' \qquad (2.1)$$

is used, with z the vertical position, θ the zenith angle of propagation direction, $T(z)$ the temperature at height z, $B(T)$ the temperature dependent emission according to Planck's law, and θ' the direction of incoming radiation that is scattered into the direction of propagation θ. For azimuthally symmetric and isotropic problems, which is also a necessary limitation for Eqn. (2.1), $\overline{\mathbf{I}}$ can be solved for without bothering about U and V. The extinction matrix $\overline{\overline{\sigma}}_e(z,\theta)$ describes the loss of radiation due to absorption and scattering. Emission is described by a vector of absorption coefficients that depend on direction and state of polarization. The phase matrix $\overline{\overline{\mathbf{P}}}(z,\theta;\theta')$ contributes to the source function, representing the amount of intensity that is scattered by hydrometeors from incoming directions θ' to the direction θ. For arbitrary conditions this system of integro-differential equations must be solved numerically.

If the size parameter $\chi = 2\pi r/\lambda \ll 1$ we are in the range of the Rayleigh approximation, where the shape of the particle is of no importance. For particles that are large compared to the wavelength ($\chi \gg 1$) the geometric optics approximation (ray tracing) may be applied. In the range of particle sizes comparable to wavelength exact solutions of Maxwell's equations have to be used, taking into account the shape of the particle.

For nonspherical particles numerical models have been developed to obtain the amplitude scattering function (a variety of methods can be found in: MISHCHENKO et al., 1999) from which all radiation interaction parameters can be calculated.

2.2 Model description

For solving the VRTE we apply the successive order of scattering (SOS) method. In the present study a set of 24 propagation directions (12 Gaussian angles per hemisphere) is used for the directional discretization of the radiation field. Although the model includes an ocean surface reflection module and a sea ice module (FUHRHOP et al., 1998), only Fresnel reflection properties are used here. The upper boundary condition is set equivalent to the cosmic background radiation of $T_{B,cosmic} = 2.7$ K. Absorption by atmospheric gases (water vapor, molecular oxygen and nitrogen) is calculated according to LIEBE et al. (1993). The single scattering properties of hydrometeors are computed by Lorenz-Mie theory in case of spheres and with the EBCM T-matrix method by MISHCHENKO (2000) when nonspherical particles are considered.

Depending on the hydrometeor species different drop size distributions (DSD) are used to estimate the polydisperse interaction parameters. For this study we use the Marshall-Palmer distribution (MARSHALL and PALMER, 1948) for precipitation particles. In case of nonspherical particles the radius of a sphere with the same volume as the spheroid is used to characterize the size of a nonspherical particle (volume equivalent radius). For simplicity the same DSD is applied for liquid and frozen precipitating hydrometeors.

We are aware of possibly more adequate size distributions for frozen particles. However, since we did not bother to obtain consistency between the relation of mass and mass fluxes for both phases we consider this an unnecessary detail. The same holds for ice particle type, which might be attributed to the nonspherical shapes. Our assumption is, that in effect our simple model is but one realization of a possible mixture of hail, graupel, and snow, which all might be present in a precipitating cloud.

Precipitating particles are always computed in the range from 100 μm to 5 mm with 50 equally spaced intervals. These intervals might be somewhat large, but they are sufficient for the purpose of this study, namely the signal reliability to be expected from influences of non-spherical particles.

When describing drop shapes, we refer to the work of CHUANG and BEARD (1990), who derived rotational symmetric shapes with cross sections $r = r(\theta)$ that can be described by a series of Chebyshev polynomials. Based on model results, the aspect ratio α, defined as the ratio of vertical and horizontal maximum extension, can be approximated by a fourth order fit depending on diameter.

For our calculations, the Chebyshev shapes are approximated by spheroids of the same volume and the same aspect ration because the single scattering model that is currently used is restricted to this more symmetric geometry. A recent study (CZEKALA et al., 1999) demonstrated that approximating the Chebyshev shapes with spheroids leads to only small errors, especially for liquid particles.

3 Theoretical results

3.1 Atmospheric conditions

We consider a very simplified rain event in the lower atmosphere. The temperature and humidity profiles are set to a mean midlatitude summer profile. Between 2 km and ground level a vertically constant rain rate is assumed. A water cloud with a LWC of 0.5 g/m^3 reaches from 1 km to cloud top of 3 km. Ice particles are placed above the 273 K isotherm (melting layer) up to a height of 3 km with the same mass per layer compared to the rain column. For both, rain and ice particles, the

Table 1: Definition of test cases.

	Shape of Raindrops	*Shape of Ice Particles*
A	Spheres	(No Ice Particles)
B	Oblate Spheroids	(No Ice Particles)
AC	Spheres	Spheres
AD	Spheres	Oblate Spheroids
BC	Oblate Spheroids	Spheres
BD	Oblate Spheroids	Oblate Spheroids

Marshall-Palmer DSD is applied by using the volume equivalent radius for nonspherical hydrometeors.

The approximation of raindrops by oblate spheroids with their rotational axis aligned to the vertical is a realistic assumption. Applying the same sizes, shapes and masses also to large precipitating ice particles is not meant as a perfect approximation to the real ice particles like hail, snow, or graupel. Our intention here is to investigate the basic effects of ice particle scattering above raining layers. Certainly the ice particle shapes vary much more than those of water drops, but the assumption of oblate particles has still some validity. The amount of ice that we use in this study is certainly rather high. For smaller ice masses the signal from the raining layers will be less disturbed by the ice scattering. With the chosen atmospheric setup, however, we are able to better understand the fundamental combined effects of rain and ice particle scattering. More realistic calculations, on which retrieval schemes may be set up, should take into account the shapes of ice particles and their vertical profiles in more detail. In addition, such calculations would also have to account for three-dimensional geometry in order to give reliable results in case of convective cells which are known to have small scales compared to the satellite field of view.

For reasons of comparison the clear atmosphere (without any hydrometeors) and the cloudy atmosphere (only the water cloud) are calculated as test cases. Radiative transfer results of the rainy atmosphere are calculated with and without an ice particle layer (Table 1). The water cloud is always present in the precipitating cases and modeled using spherical particles.

All six situations were calculated for two different surface conditions and a variation of the rain rate between 0 and 100 mm/h. We are aware of the fact that the rain rates at the high end become inconsistent with the assumed non-raining cloud, but since only possible effects are addressed, we consider this as not important. Using the surface emissivity $\varepsilon = 1.0$ assumes a perfect black body and results in a strong unpolarized surface emission. It allows us to study the polarization effects of the hydrometeors without polarization effects by the surface, which is typical for land surfaces. Alternatively, the frequency dependent reflection of a flat water surface is used to study the polarization effects in the presence of large PD from surface emission.

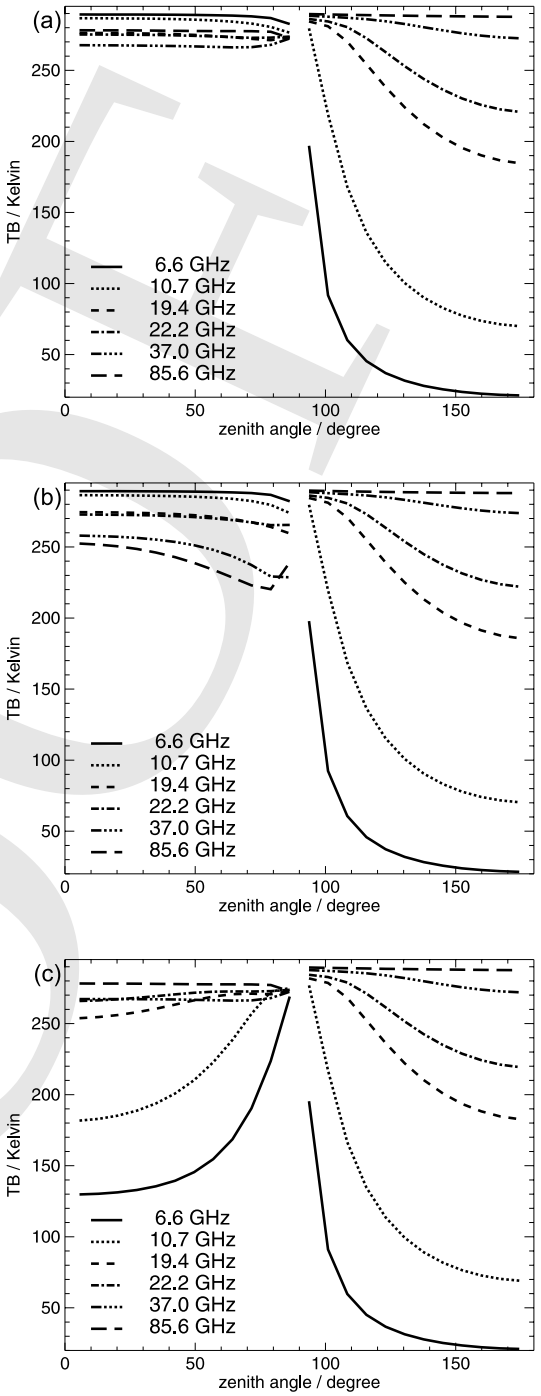

Figure 1: Total brightness temperature $T_B = (T_{B,v} + T_{B,h})/2$ versus zenith angle of propagation at different frequencies for 20 mm/h rain rate. Three different situation are shown: case B with emissivity set to $\varepsilon = 1.0$ (a), case BD with $\varepsilon = 1.0$ (b), case B with polarizing sea surface below (c).

3.2 Angular dependence

The variation of total intensity with zenith angle for oblate rain particles without ice (case B) is shown in Fig. 1a for a rain rate of 20 mm/h and $\varepsilon = 1.0$. Angles less

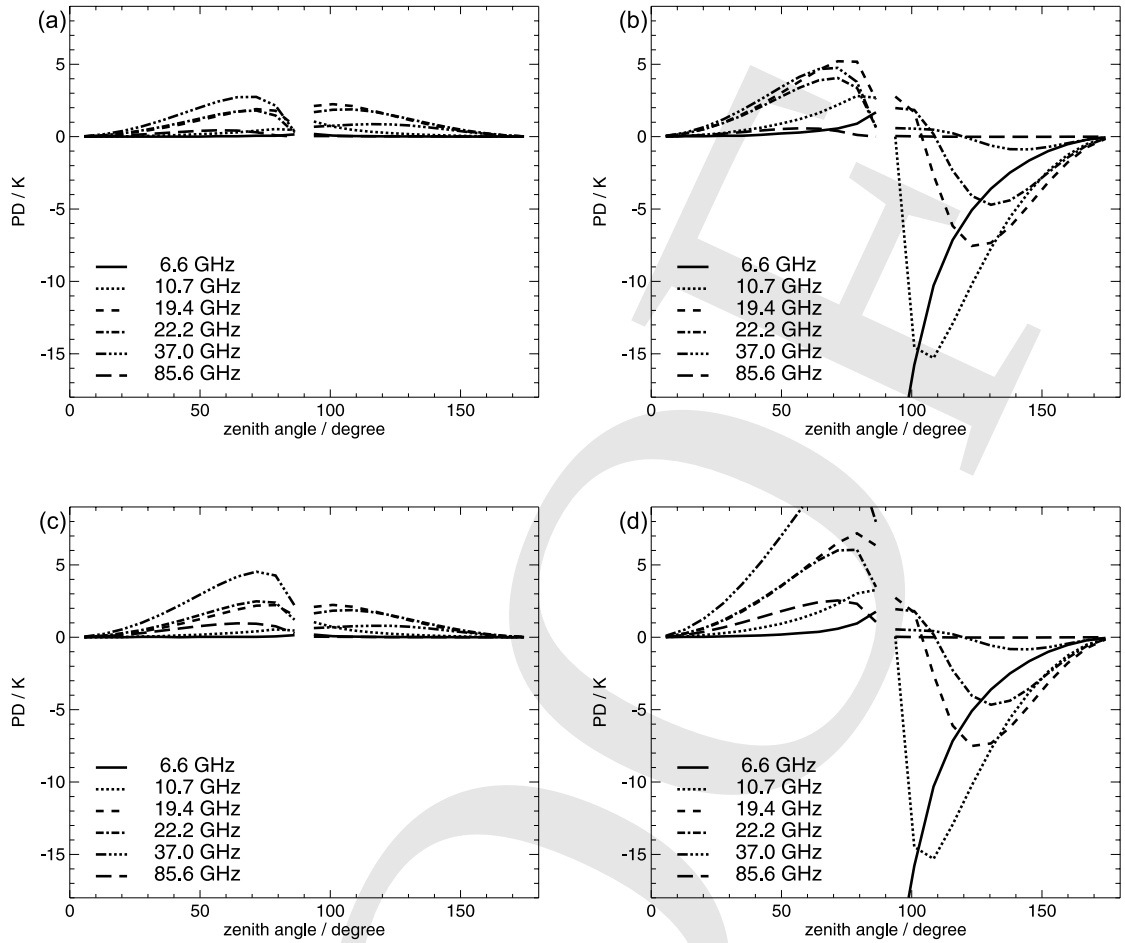

Figure 2: Angular dependence of PD for different cases, all with $\varepsilon = 1.0$ and RR = 20 mm/h: (a) case A, (b) case B, (c) case AC, (d) case BD.

than 90° relate to observations from space (e.g. satellite observations), while larger angles show the downwelling radiances at the surface (e.g. observations by a ground based radiometer).

When observing the atmosphere from above, the main contribution is the thermal emission from the surface. With increasing opacity to higher frequencies the radiation originates from higher layers of the atmosphere, reducing T_B. For downward directions we see that for this case the atmosphere is partly transparent for the lower four frequencies. Due to the small signal from space and only small contributions from the atmosphere the resulting T_B remains rather cold.

Adding a further precipitating layer with ice particles of the same precipitation rate from 2 km to 3 km height (case BD, Fig. 1b) leaves the results for downward directions nearly unchanged. The upwelling radiation is affected by the brightness temperature depression due to scattering, showing the highest efficiency at 85 GHz.

Fig. 1c shows the effect of sea surface emission/reflection. The mean emissivity is significantly smaller than one, leading now to lower brightness temperatures also at upward directions. For long optical path lengths (angles close to the horizontal) and also at higher frequencies the atmosphere becomes opaque enough to cause T_B to be close to the physical temperature of the layers in the upper atmosphere.

Figs. 2a to 2d give the resulting PD from four calculations with 20 mm/h rain rate and black body surface emission ($\varepsilon = 1.0$). The atmospheric conditions are set to the cases A, B, AC, and BD, respectively (Tab. 1). The most evident feature for nonspherical particle shapes (cases B and BD) is the negative PD at downward directions. This feature may have large impacts on ground based observations. The details have been discussed elsewhere (CZEKALA and SIMMER, 1998; CZEKALA et al., 2001a,b).

The PD which an airborne sensor would observe is always positive, but smallest for the spherical rain particles without ice (case A, Fig. 2a). At the SSM/I observation angle (53°) and with so far assumed atmospheric conditions the 37 GHz signal shows the largest PD compared to other channels. Oblate raindrops result in an enhanced PD in upward directions, especially for the 19, 22, and 37 GHz channels (case B, Fig. 2b). Adding ice particles increases the positive PD for spherical particles (case AC, Fig. 2c), but this behavior is even stronger for oblate ice particles (case BD, Fig. 2d). The observed PD increases with zenith angle until the atmosphere becomes opaque near the horizontal direction. This point

of saturation is reached for the higher frequencies at smaller zenith angles, with no saturation at all for 6.6 and 10.7 GHz.

Polarization at the top of the atmosphere due to ice particle scattering is most efficient at 37 GHz with the above choice of ice particle shape. However, the reported SSM/I observations of PD above mesoscale convective systems state that the PD signature at 85 GHz very often is larger than at 37 GHz (HEYMSFIELD and FULTON, 1994). Possible reasons for this discrepancy are:

(1) The modeled 85 GHz polarization difference is too small because of the assumed quite spherical ice particle shape. The shape would affect the 85 GHz signal more than the 37 GHz signal due to the larger size parameter for the single scattering calculations. The 37 GHz signal is also sensitive to the liquid phase (while the liquid phase has no significant effects on the 85 GHz channel due to high absorption).

(2) The optical thickness at 85 GHz due to gas absorption and the water cloud in the atmospheric layers containing the oblate ice particles is too high. This leads to a saturated and thus more isotropic distribution of radiation at 85 GHz with only very small amounts of PD. At 37 GHz the transparency of the cloudy atmosphere is still large enough to produce significant amounts of PD.

(3) Averaging over the field of view in satellite observations will decrease the precipitation induced signal because in most cases the antenna pattern will be filled with raining and non-raining areas (or areas with smaller rain rates than the maximum rain rate). The observed signal of the inhomogeneous scene is a non-linear mixture of several rain rates. This effect of inhomogeneity is more pronounced for the lower frequencies due to their increased footprint size. Thus the strong signal calculated for 37 GHz and a high rain rate in a one-dimensional atmosphere would only be received if the rain rate is constant within an area from which most of the total signal originates (about 74×58 km for 37 GHz and 30×26 km for 85 GHz).

(4) In this study we assume perfect alignment of the oblate particles and thereby overestimate the generation of polarization. The ice particles introducing a polarization signal at 85 GHz also include smaller ice crystals which are not large enough to be effective scatterers at 37 GHz. For particles the assumption of horizontal alignment is more justified than for large particles (hail, snow), which are more likely to show tumbling. However, recent investigations by PRIGENT et al. (2000) assess the influence of semi-random orientation in more detail. They demonstrate that a variation of the particles rotational axis within $+/-10^{o}$ off the vertical alters the polarization induced by oblate ice particles only by about 10%.

In addition to the above explanations we want to make clear that a reproduction of the results reported by HEYMSFIELD and FULTON (1994) can be achieved with different atmospheric definitions: When using more oblate shapes for ice particles or when placing the ice particles in colder atmospheres or at higher altitudes the PD at 85 GHz increases (see Section 3.4). The precise influence of ice particle shape on the polarization, especially at 37 and 85 GHz, will be investigated later in this study.

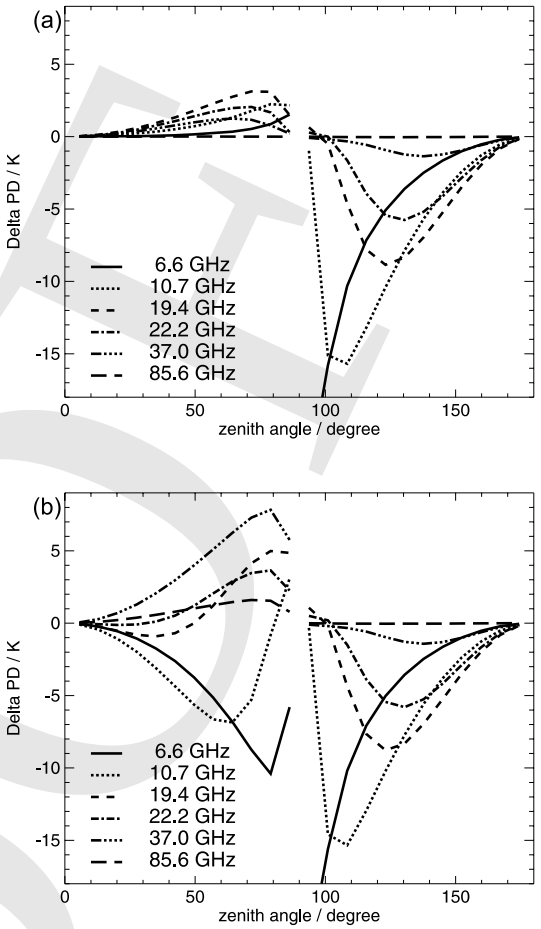

Figure 3: (a) Change in PD (ΔPD=PD$_{BD}-$PD$_{AD}$) when using oblate particle shape for both phases (case BD) instead of spherical rain and oblate ice particles (case AD). The rain rate is set to 20 mm/h, the surface emissivity to $\varepsilon = 1.0$ in both cases. (b) Change in PD (ΔPD=PD$_{BD}-$PD$_{AC}$) when using oblate shapes for both phases (case BD) instead of spheres for both (case AC). The rain rate is set to 20 mm/h, but the surface emissivity is set to Fresnel reflection.

A closer look on the difference of two calculations shows that the PD originating from the liquid hydrometeors can be seen from above even through the layer of ice particles (Fig. 3). Both calculations were carried out with 20 mm/h rain rate and an emissivity of $\varepsilon = 1.0$, one using oblate shapes for both liquid and frozen particles, the other one using oblate ice particles but spherical rain drops. We refer to the resulting change in PD as ΔPD=PD$_{oblate}-$PD$_{spheres}$. In the following ΔPD will always designate the result of subtracting spherical results from nonspherical results. The effect in ΔPD is very close to the difference of oblate and spherical particles in the absence of the ice layer, pointing out the need of taking the shape of raindrops into account even when hidden by an ice layer above.

By switching the surface emissivity to sea surface conditions the observed PD at upward directions is dominated by the polarized surface. This effect produces for example a PD up to 60 K at the top of the atmosphere for 10.7 GHz and will not be totally damped by the rain mass within the atmosphere. However, the PD generation by rain and ice layers is still observable in the difference of the more realistic shapes (case BD, both phases with oblate particles) and the simplified assumption (case AC, both phases modeled as spheres) (Fig. 3b).

In contrast to cases with $\varepsilon = 1.0$ the transition from spherical to nonspherical oblate particle shape does not increase the PD at all frequencies. Instead, at some frequencies the upwelling PD is enhanced by nonsphericle particle shape (positive ΔPD for 85, 37, and 22 GHz) while at others the PD is lowered (negative ΔPD for 10.7 and 6.6 GHz). At 19 GHz both enhancement and decrease of PD take place, depending on the angle of observation.

The angle and frequency dependence of this result can be reduced to the question of total optical thickness and its effect on the distribution of radiation. At higher frequencies the lower atmosphere is opaque and therefore acts similar to a warm black body surface: The amount of upwelling radiation is large in all upward directions from 0 to 90 degrees. At low frequencies the surface emitted radiation is roughly half the amount at black body conditions. Additional amounts of radiation are emitted by the atmosphere itself. For directions close to the horizontal the optical path is geometrically increased and the brightness temperature raised to amounts close to ambient physical temperatures.

This self-emission of the atmosphere increases with increasing angle and increasing frequency and therefore generates a more isotropic radiation field. Only in case of non-isotropic radiation negative PD is produced. At 10.7 and 19 GHz the situation changes from non-isotropic to isotropic with increasing angle of observation. At 85 GHz again the optical thickness within the lower layer of this model atmosphere is too large to produce any significant upward directed polarization effects.

This change in PD is not originating from the polarized emission of the surface but from the changed intensity distribution caused by the lowered emissivity of the ocean surface. This was proven by reproducing similar changes in ΔPD for the same atmospheric conditions but using a Lambertian (non-polarizing) surface with a similarly low emissivity as the ocean (see Fig. 9a and Fig. 9b in CZEKALA et al. (1999)).

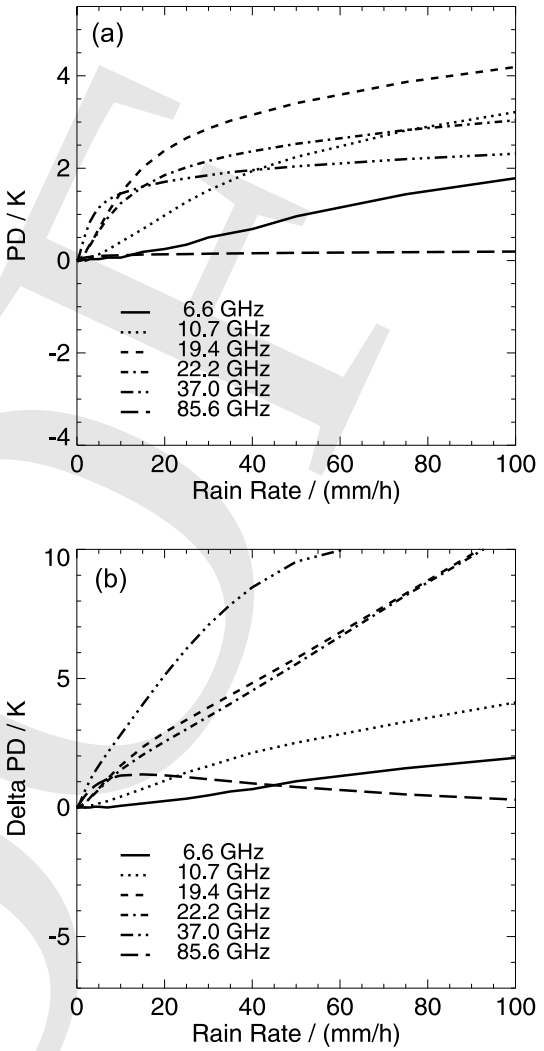

Figure 4: (a) PD versus rain rate for different frequencies (case B, rain layer with oblate spheroids, viewing angle of 56 degrees and black body surface $\varepsilon = 1.0$). (b) Change in PD (ΔPD=PD$_{BD}$−PD$_{AC}$) versus rain rate when using oblate raindrops and ice particles (case BD) instead of spheres for both (case AC) at a viewing angle of 56 degrees and black body surface $\varepsilon = 1.0$.

3.3 Rain rate dependence

The results presented so far were calculated with a fixed rain rate of 20 mm/h. Fig. 4a shows the PD produced by a liquid rain layer above a black body emitting surface (case B) versus the rain rate for a zenith angle of 56 degrees. The resulting PD clearly depends on the optical thickness produced by the water mass in the atmosphere. The sensitivity to rain rate (indicated by the slope of the curves for the lowest rain rates) is increasing with with frequency, but saturation is reached at decreasing rain rates for increasing frequencies. A special situation is observed for 85 GHz: The optical thickness due to cloud water, gas absorption and a minimum amount of rain leads to an optical thickness large enough to produce a fully isotropic radiation field within the rain layers. Thus no PD is produced for pure rain layers with this atmospheric setup.

The difference of PD calculated with non-spherical rain and ice particles on the one hand and spherical particles on the other hand (ΔPD=PD$_{BD}$−PD$_{AC}$) also varies with rain rate (Fig. 4b). ΔPD is highest for 19, 22, and especially 37 GHz. Above sea surfaces and at low rain rates PD is dominated by the surface induced polariza-

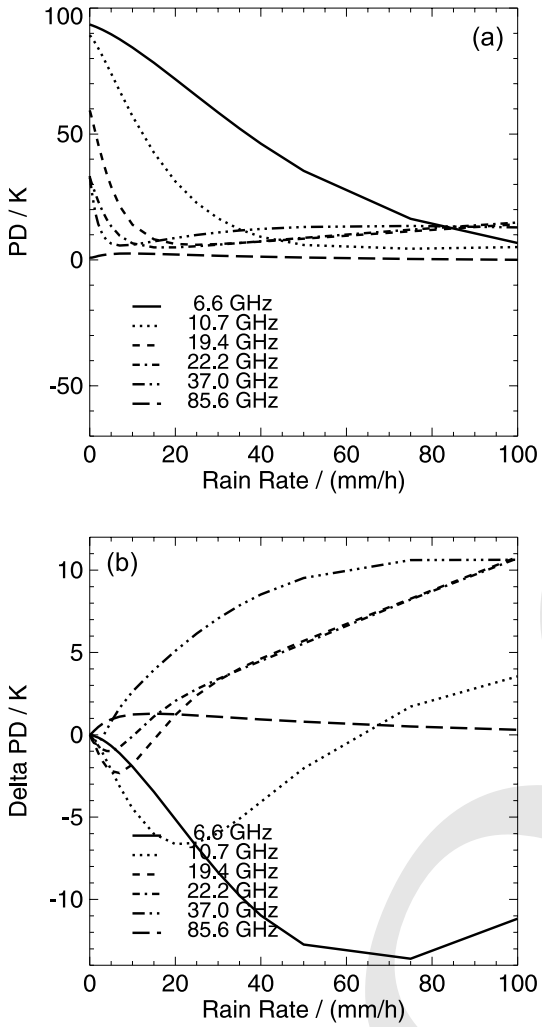

Figure 5: (a) PD versus rain rate over water surface. Oblate raindrops and oblate ice particles are used (case BD). (b) Corresponding change in PD (ΔPD=PD$_{BD}-$PD$_{AC}$) versus rain rate when using oblate raindrops and ice particles (case BD) instead of spheres for both (case AC). This is similar to Fig. 4, but with sea surface emission.

tion (Fig. 5a). With increasing rain rate the atmosphere becomes opaque and PD is damped. After saturation (when no PD from the surface is reaching the cloud top) we observe again increasing PD which is induced by scattering of the upwelling radiation by nonspherical hydrometeors of both phases, liquid and frozen. At 25 mm/h the PD at 37 GHz reaches 10 K, which totally originates from hydrometeors.

Finally, the changes in PD when using the oblate shapes instead of the spherical shapes over water surfaces (Fig. 5b) is much more complicated than in the case of perfect black body emission (Fig. 4b). For optically thick atmospheres the radiation is close to isotropic and additional positive PD is produced by oblate particles. At low opacities the non-isotropic conditions in the upwelling radiation produced by the sea surface cause additional negative PD. It is important to understand that the non-isotropic radiation will produce negative PD only in combination with oblate particles. Spherical particles always lead to a positive PD. At small rain rates simulations with spherical particles will overestimate PD. The reason is that nonspherical particles produce negative PD in a situation when the intensity distribution is highly non-isotropic due to the lowered ocean emission. This negative PD leads to a decrease of the large positive PD from the surface. Scattering at spherical particles will not produce this negative fraction of PD and therefore the resulting ΔPD is larger.

With increasing opacity caused by increasing rain rate the atmosphere becomes opaque, the intensity distribution becomes more isotropic and the negative PD caused by nonspherical particles changes to positive values. This point is reached at lower rain rates for higher frequencies. Further increase of rain rate makes the surface invisible from above. The only resulting PD (at frequencies above 10.7 GHz) is then produced by the hydrometeors. In this situation the nonspherical particles polarize the radiation more efficiently than spheres. Calculations neglecting the aspherical shape will underestimate the PD.

3.4 Comparison to reported polarization signatures

Residual polarization differences above optically thick precipitation events have been reported by a number of researchers (SPENCER et al., 1989; HEYMSFIELD and FULTON, 1994; PETTY and TURK, 1996). In the documented cases the PD at 85 GHz reached values of about 5 to 13 K with smaller amounts (up to 7 K) for 37 GHz. They all speculated that this PD is caused by nonspherical oblate ice particles. Modeling efforts have been made to confirm these observations. Model results (PETTY and TURK, 1996; HAFERMAN, 1999) support the assumption that large oblate ice particles produce the positive PD found at 85 GHz.

Recently, there has been an approach by ROBERTI and KUMMEROW (1999) (hereafter RK99) to reproduce the observations at 37 and 85 GHz reported by HEYMSFIELD and FULTON (1994) with a one-dimensional radiative transfer model and model output from an atmospheric mesoscale model (MM). The MM output specified the mass of cloud water, cloud ice, rain, graupel, and snow in each layer. The shape of rain drops and graupel is assumed to be spherical, while snow particles were modeled as nonspherical particles. They succeeded to obtain results consistent with the observations after changing some microphysical parameters (the aspect ratio used for the oblate snow particles and the percentage of the spherical graupel additionally converted to snow) based on a sensitivity study: From the variation of the graupel-to-snow conversion rate (0 to 100%) and aspect ratio (2.0 to 5.0) those parameters were chosen that explained the observations of HEYMSFIELD and FULTON (1994). They state *To obtain the desired* ΔT_{V-H} *in the anvil, the content of snow originally present in the*

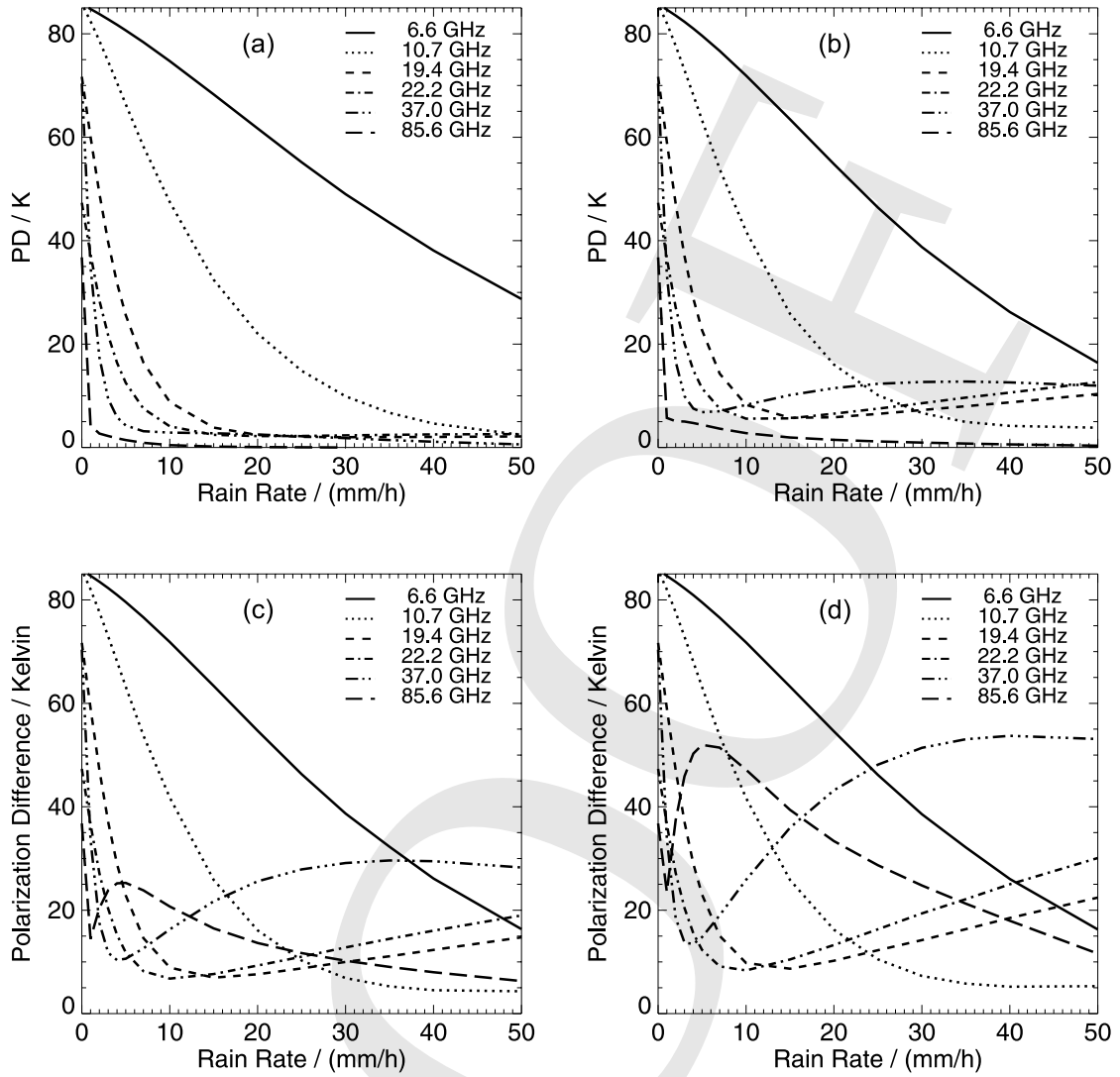

Figure 6: Dependence of PD on RR over polarizing sea surface for a viewing angle of 56 degrees for different selections of particle shape (for details see text): (a) spherical rain and spherical ice particles, (b) nonspherical rain and ice particles of Type-I, (c) nonspherical rain and ice particles of Type-II, (d) nonspherical rain and ice particles of Type-III are used.

cloud seems to be too low. It is necessary to transform 50% of the graupel to snow to start obtaining ΔT_{V-H} *of 11 K at 85 GHz with* $\Delta T_{V-H} < 6\,K$ *at 37 GHz.* (ROBERTI and KUMMEROW, 1999, p. 2101). No microphysical explanation is offered. So the main conclusion from this paper is that oriented oblate ice particles lead to positive PD for spaceborne observations, which is consistent with other studies on this topic (EVANS and STEPHENS, 1995b; CZEKALA, 1998).

However, there are two limitations in the study of RK99. First, the numerical noise of roughly 2 K in the calculated TB and PD of RK99 mask the results for small snow densities (their Figs. 3, 4, and 5). Second, the model results for oriented oblate particles presented in RK99 were calculated with a one-dimensional radiative transfer model that mixed single scattering parameters of randomly oriented particles (computed with a T-Matrix code which was restricted to randomly oriented particles) and perfectly aligned particles (calculated with the discrete dipole approximation).

This simplification is not well justified since the interaction of relative high upwelling brightness temperature with ice particles is largely affected by the extinction. In addition, for oriented nonspherical particles angle dependent matrices have to be used (see Eqn. (2.1)).

Another recent study (PRIGENT et al., 2000) investigates the residual polarization difference found in tropical SSM/I observations. They report that the PD over ocean never reaches zero for 37 and 85 GHz, which obviously supports also our findings of hydrometeor generated PD. PRIGENT et al. (2000) also support their analysis of SSM/I data with model calculations of oblate ice particles above spherical rain particles. They assume rotationally symmetric particles with a random distribution of their rotational axis in the azimuthal plane. The distribution of the particles axis in the zenith direction

is continuously varied, covering all distributions from perfect alignment to random orientation. They conclude that oriented ice particles are capable of generating the observed positive PD, while randomly oriented particles are not.

Our calculations generally produced small or vanishing positive PD at 85 GHz, but noticeable PD at 37 GHz. This is caused by our model atmosphere which assumed (1) ice particles with small nonsphericity (same aspect ratios as the water drops), (2) a low melting layer height which results in a significant absorption at 85 GHz above the precipitation by the remaining atmosphere, and (3) a small vertical extension of the layers containing the frozen precipitation: Only within 1 km ice particles were present.

The above assumptions are realistic for some weather conditions at mid and high latitudes, but naturally will not produce a large scattering signal at 85 GHz. The following calculations were performed with a different atmospheric structure that contained also more frozen hydrometeors. The sea surface temperature is 293 K, the melting layer with 273 K is located at 3 km. Below 3 km a vertically constant rain rate is assumed. From 3 to 4 km precipitation is split into a mixture of liquid and frozen precipitation. From 4 to 6 km only frozen precipitation particles are used. A calm water surface (Fresnel reflection) is used at the lower boundary. Rain is modeled as before, but three different ice particle types are used: The same size-dependent aspect ratio as used for rain ("Type-I", equivalent to the prior computations), a fixed aspect ratio of 1.7 (which means oblate particles) for all sizes of hydrometeors ("Type-II"), and a fixed aspect ratio of 3.0 also regardless of particle size ("Type-III"). These choices are not meant to be valid descriptions of the hydrometeor type that can be found in graupel, hail, or snow, but they bear some relation to the parameters of natural ice particles in clouds and allow for a rough estimation of the extremes that may affect the rain retrieval.

The rain rate dependence of the PD was recalculated over an ocean surface using four scenarios: (a) spherical particles for rain and ice (Fig. 6a), (b) oblate rain and Type-I ice particles (Fig. 6b), (c) oblate rain and Type-II ice particles (Fig. 6c), and (d) oblate rain and Type-III ice particles (Fig. 6d). All 4 calculations show the reduction of surface produced PD with increasing optical thickness. The full spherical calculation (Fig. 6a) reveals the smallest PD after saturation, but saturation is reached at very high rain rates for 10.7 GHz and no saturation at all occurs at 6.6 GHz.

With nonspherical rain and nonspherical ice particles of increasing nonsphericity of the ice particles (Figs. 6b–6d) the PD is increased at the four higher frequencies, but with different sensitivity. Especially 37 and 85 GHz show a strong response. While for spherical particles and the least nonspherical particles of Type-I the 85 GHz PD is always smaller than the 37 GHz signal, the situation is reversed for ice particles of Type-II and Type-III for moderate rain rates up to 10 and 15 mm/h, respectively. This is a reasonable range for average rain rates in a satellite field of view.

For the lowest two frequencies (6 and 10 GHz) a decrease in PD takes place. This decrease is not due to a more efficient screening of the surface PD but due to the additional negative PD produced by the nonspherical particles in semi-transparent atmospheres with low surface emissivity. This negative PD is also produced by the hydrometeors when using a non-polarizing surface with the same average emissivity instead of the polarizing sea surface. It is obvious that low frequencies are much less affected by ice particle shape. At 6 and 10 GHz the results are identical and for the intermediate frequencies of 19 and 22 GHz the change in PD is still small. But at 37 and 85 GHz the PD entirely depends on ice particle shape.

It is worth to mention that the low frequencies are perfectly insensitive to ice particle shape, but not to rain particle shape (comparison of Fig. 6a and Fig. 6c). There is a significant difference in the PD at 6 and 10 GHz that is arising only due to nonspherical water drops below a very large ice particle layer.

4 Discussion

Our results demonstrate that rain and ice particle shape both have an impact on the polarization difference as observed from a spaceborne sensor, leaving the average brightness temperature almost unaffected. Since the vertically and horizontally polarized signals are influenced in different ways by interaction with the hydrometeors, a thorough knowledge of the origin of the PD signal is essential to understand the pattern of multi-channel results. Even if the PD is not explicitly used in a retrieval process, the measured radiances are always polarized measurements and therefore depend on polarization effects within the atmosphere.

The PD produced by the hydrometeors within the atmosphere always adds up with PD that originates from surface effects. This effect is stronger for scattering by large oblate ice particle in large altitudes, but also observed at all other frequencies and for liquid hydrometeors. In fact, the PD signal introduced by oblate raindrops is observable at low frequencies even if the rain layer is covered by large amounts of ice. In addition, the specific shape of the ice particles has only a small impact on the signal at low frequencies. As a consequence, the polarization signal at low frequencies contains direct information about the rainfall intensity itself. With a knowledge of the ocean surface properties and an understanding of the connection between PD and precipitation this knowledge can possibly help to improve the quality of precipitation retrieval.

Up to now the hydrometeor-induced PD (including the effects of particle nonsphericity) is not accounted for in multi-channel approaches of microwave rain retrieval. Furthermore, those precipitation retrievals which rely on the 85 GHz scattering signature as the main source of

information, depend on a precise knowledge of ice particle shape. If the ice particle shape is not known then the interpretation of the observed radiances is at least dangerous. Different types of precipitation may be associated with hail stones, large snow flakes, graupel, melting particles, small ice crystals, mixtures of all, or no ice at all (warm rain). Thus the performance of scattering based retrievals depends possibly more on the type of precipitation event than on precipitation intensity. In addition, the correlation between the ice which is present above the melting layer and the rainfall rate is imperfect, which again emphasizes the need of using the information that is contained in the low frequency PD. This information is directly linked with the rain signal due to the larger transparency of the atmosphere and the better known shape of raindrops.

Our calculations use ice particle shape and vertical profiles that are artificially created. Nonetheless this atmospheric setup is not unphysical because all parameters are varied in reasonable intervals. Our results for the different ice particle shapes indicate the range of the PD that may be produced by different types of rain and point out the problems that arise when focusing on this sensitive signal.

From this simple setup much can be learned for the understanding of how the observed signals are generated by the atmosphere. However, there are still improvements to be made. A variation of particle size distributions, ice particle density, explicit treatment of the melting layer, and three-dimensional geometry were neglected in this study. These shortcomings are not expected to alter the overall conclusions. A decreased particle density together with adjusted fall velocity will lead to an significant increase in particle number in order to obtain the mass flux of precipitation above and below the melting layer. These increased numbers of scattering particles will increase the resulting PD. The same is expected for the melting layer which contains large nonspherical melting particles which very effectively scatter and emit microwave radiation due to their size and refractive index, which varies with the mixing of ice, air, and water. While the permittivity and density changes of melting particles have been investigated (BAUER et al., 2000), the combined effects with nonsphericity of melting ice particles have not been investigated up to now. On the contrary, there are other effects which will lead to some decrease of the expected polarization effects. Non-perfect orientation of the particles will smooth the results somehow, as will drop oscillations and tumbling of the particles. The effects of ice particle vertical alignment in the electrical field within a thunderstorm has also not been considered by now.

5 Summary and conclusions

We have used a one-dimensional microwave vector radiative transfer model to calculate the effects of nonspherical hydrometeors with fixed orientation on satellite observed microwave radiation. The model shows good agreement with ground based measurements (CZEKALA et al., 2001a) which confirm the correct treatment on nonspherical precipitation. The model calculated polarization signatures are discussed and compared with reported observations and other model results.

By using different surface boundary conditions and atmospheric compositions we showed that the polarization difference produced by oblate particles is generally larger than for spherical particles. However, this result is reversed for the lowest frequencies together with small surface emissivities. Low frequencies are very sensitive to the liquid part of the precipitation, high frequencies to the ice phase. The PD produced by rain in the low frequencies is only little changed by ice layers above and can be observed even in the presence of large ice masses.

Surface generated polarization and hydrometeor generated polarization add up to a combined signal. Identifying the different contributions is crucial for microwave rain retrievals. Using all available information contained in multi-frequency microwave measurements is essential. Focusing only on the 85 GHz scattering signature may be misleading due to the very strong sensitivity to particle shape. The a-priori unknown ice particle shape makes this signal ambiguous and suggests the additional use of the smaller but less ambiguous signals at low frequencies with the correct treatment of rain drop shape and orientation.

Acknowledgments

This work was supported by the Deutsche Forschungsgemeinschaft under contract Si 606/1-1 and 606/1-2. We thank Michael MISHCHENKO for making available the EBCM T-matrix code. We thank Jeffrey HAFERMAN, Catherine PRIGENT and Bill ROSSOW for helpful comments.

References

ADLER, R.F., A.J. NEGRI, P. KEEN, I.M. HAKKARINEN, 1993: Estimation of monthly rainfall over Japan and surrounding waters from a combination of low-orbit microwave and geosynchronous IR data. – J. Appl. Meteorol. **32**, 335–356.

ASANO, S., G. YAMAMOTO, 1975: Light scattering by a spheroidal particle. – Appl. Opt. **14**, 29–49.

BAUER, P., A. KHAIN, A. POKROVSKY, R. MENEGHINI, C. KUMMEROW, F. MARZANO, J.P.V.P. BAPTISTA, 2000: Cloud-microwave radiative transfer modeling of stratiform rainfall. – J. Atm. Sci. **57**, 1082–1104.

CHUANG, C., K.V. BEARD, 1990: A numerical model for the equilibrium shape of electrified raindrops. – J. Atm. Sci. **47**, 1374–1389.

CZEKALA, H., 1998: Effects of ice particle shape and orientation on polarized microwave radiation for off-nadir problems. – Geophys. Res. Lett. **25**, 1669–1672.

CZEKALA, H., S. CREWELL, A. HORNBOSTEL, A. SCHROTH, C. SIMMER, A. THIELE, 2001a: Interpretation of polarization features in ground based microwave observations as caused by horizontally aligned oblate rain drops. – J. Appl. Meteorol. **40**, 1918–1932.

CZEKALA, H., S. CREWELL, C. SIMMER, A. THIELE, 2001b: Discrimination of cloud and rain liquid water path by groundbased polarized microwave radiometry. – Geophys. Res. Lett. **28**, 267–270.

CZEKALA, H., S. HAVEMANN, K. SCHMIDT, T. ROTHER, C. SIMMER, 1999: Comparison of microwave radiative transfer calculations obtained with three different approximations of hydrometeor shape. – J. Quant. Spectrosc. Radiat. Transf. **63**, 545–558.

CZEKALA, H., C. SIMMER, 1998: Microwave radiative transfer with non-spherical precipitating hydrometeors. – J. Quant. Spectrosc. Radiat. Transf. **60**, 365–374.

EVANS, K.F., G.L. STEPHENS, 1995a: Microwave radiative transfer through clouds composed of realistically shaped ice crystals. Part I: Single scattering properties. – J. Atm. Sci. **52**, 2041–2057.

—,— 1995b: Microwave radiative transfer through clouds composed of realistically shaped ice crystals. Part II: Remote sensing of ice clouds. – J. Atm. Sci. **52**, 2058–2072.

EVANS, K.F., S.J. WALTER, A.J. HEYMSFIELD, M.N. DEETER, 1998: Modeling of submillimeter passive remote sensing of cirrus clouds. – J. Appl. Meteorol. **37**, 184–205.

FUHRHOP, R., T.C. GRENFELL, G. HEYGSTER, K.-P. JOHNSON, P. SCHLÜSSEL, M. SCHRADER, C. SIMMER, 1998: A combined radiative transfer model for sea-ice, free ocean and atmosphere. – Radio Science **33**, 303–316.

HAFERMAN, J.L., 1999: Microwave Scattering by Precipitation. – In: Light Scattering by Nonspherical Particles: Theory, Measurements, and Applications, MISHCHENKO, M.I., J.W. HOVENIER, L.D. TRAVIS (Eds.), Academic Press, San Diego, California, USA, 481–524.

HAFERMAN, J.L., T.F. SMITH, W.F. KRAJEWSKI, 1997: A multi-dimensional discrete-ordinates method for polarized radiative transfer. Part I: Validation for randomly oriented axisymmetric particles. – J. Quant. Spectrosc. Radiat. Transf. **58**, 379–398.

HEYMSFIELD, G.M., R. FULTON, 1994: Passive microwave and infrared structure of mesoscale convective systems. – Meteorol. Atm. Phys. **54**, 123–139.

HORNBOSTEL, A., A. SCHROTH, A. SOBACHKIN, B. EVTUSHENKO, G. ZAGORIN, 1999: Passive and active stokes vector measurements of microwave emission and scattering by precipitation. – In: IGARSS'99, 28 June–2 July 1999, Hamburg, Germany, Proceedings, 2078–2080.

LIEBE, H.J., G.A. HUFFORD, M.G. COTTON, 1993: Propagation modeling of moist air and suspended water/ice particles at frequencies below 1000 GHz.. – In: AGARD 52nd Specialists Meeting of the Electromagnetic Wave Propagation Panel, Palma de Mallorca, Spain. **Veranstaltungsdatum? Welche Seiten?**

LIU, Q., C. SIMMER, 1996: Polarisation and intensity in microwave radiative transfer. – Contr. Atm. Phys. **69**, 535–545.

MARSHALL, J.S., W. PALMER, 1948: The distribution of raindrops with size. – Meteorology **5**, 165–166.

MISHCHENKO, M.I., 2000: Calculation of the amplitude matrix for a nonspherical particle in a fixed orientation. – Appl. Opt. **39**, 1026–1031.

MISHCHENKO, M.I., L.D. TRAVIS, A. MACKE, 1999: T-Matrix method and its applications. – In: Light Scattering by Nonspherical Particles: Theory, Measurements, and Applications, MISHCHENKO, M.I., J.W. HOVENIER, L.D. TRAVIS (Eds.), Academic Press, San Diego, California, USA, 147–172.

OGUCHI, T., 1960: Attenuation of electromagnetic wave due to rain with distorted raindrops. – J. Radio Res. Lab. **7**, 467–485.

— 1964: Attenuation of electromagnetic wave due to rain with distorted raindrops (Part II). – J. Radio Res. Lab. **7**, 19–44.

PETTY, G.W., J. TURK, 1996: Observed multichannel microwave signatures of spatially extensive precipitation in tropical cyclones. – In: 8th Conf. Sat. Meteorol. Oceanogr., Preprints, Atlanta, GA, 291–294. **Konferenzdatum? War es eine AMS-Konferenz?**

PRABHAKARA, C., G. DALU, R. SUSHANISI, J.J. NUCCIARONE, G.L. LIBERTI, 1992: Rainfall over oceans: Remote sensing from satellite microwave radiometers. – Meteorol. Atm. Phys. **47**, 177–199.

PRIGENT, C., J.R. PARDO, M.I. MISHCHENKO, W.B. ROSSOW, 2000: Microwave polarized scattering signatures in clouds: SSM/I observations with radiative transfer simulations. – J. Geophys. Res. **106**, 28,243–28,258.

ROBERTI, L., C. KUMMEROW, 1999: Monte Carlo calculations of polarized microwave radiation emerging from cloud structures. – J. Geophys. Res. **104**, 2093–2104.

SPENCER, R.W., H.M. GOODMAN, R.E. HOOD, 1989: Precipitation retrieval over land and ocean with the SSM/I: Identification and characteristics of the scattering signal. – J. Atm. Sci. **6**, 254–273.

TSANG, L., J.A. KONG, R. T. SHIN, 1985: Theory of Microwave Remote Sensing. – John Wiley & Sons, 613 pp.

WU, R., J. A. WEINMAN, 1984: Microwave radiances from precipitating clouds containing aspherical ice, combined phase, and liquid hydrometeors. – J. Geophys. Res. **89**, 7170–7178.